Hydrodynamics of narrow-tube fixed bed reactors filled with Raschig rings

Moghaddam, E. M.; Foumeny, E. A.; Stankiewicz, A. I.; Padding, J. T.

Important note
To cite this publication, please use the final published version (if applicable).
Please check the document version above.

Hydrodynamics of narrow-tube fixed bed reactors filled with Raschig rings

E.M. Moghaddam *, E.A. Foumeny, A.I. Stankiewicz, J.T. Padding

Process & Energy Department, Delft University of Technology, the Netherlands

ABSTRACT

The local flow structure and pressure drop in random packings of Raschig rings are analyzed using sequential Rigid Body Dynamics (RBD) method and Computational Fluid Dynamics (CFD) simulation. Tube-to-pellet diameter ratios, N, between 3 and 6 are investigated for laminar, transitional and turbulent flow regimes ($5 \leq \mathrm{Re_p} \leq 3,000$). The computed pressure drops are in good agreement with the empirical correlation of Nemec and Levec (2005), while the Ergun equation exhibited high deviations of more than 60%, even when it is modified to explicitly account for non-sphericity of pellets. This deviation is ascribed to additional sources for eddy formation offered by Rashig rings, compared to spheres and cylinders, which cannot be counterbalanced by the usage of a higher specific surface area. The 3D results of flow structure demonstrate a large influence of packing topology on the velocity distribution: rings oriented parallel to the flow accelerate the local velocity through their axial holes, while rings oriented perpendicular to the flow provide additional space for vortex formation. The flow fields are substantially different from that found in packings of spheres and cylinders, both in terms of volume of backflow regions and velocity hotspots. This implies a higher order of local flow inhomogeneity in azimuthal and axial directions compared to spherical and cylindrical packings. Furthermore, it is found that azimuthal averaging of the 3D velocity field over the bed volume, which has been used to improve classical plug-flow pseudo-homogenous models to account for the role of tortuous velocity fields, cannot reflect the appearance of vortex regions and thereby leads to underestimation of the local axial velocity values by over 500% of the inlet velocity.

© 2020 The Author(s). Published by Elsevier Ltd. This is an open access article under the CC BY license (http://creativecommons.org/licenses/by/4.0/).

1. Introduction

Tubular fixed bed reactors with a relatively low tube-to-pellet diameter ratio N in the range of 2 to 10, are extensively employed in process and chemical industries due to their potential to enhance lateral heat transfer which is essential to prevent runaway reaction conditions and hot spot/cold spot formations. The design of such reactors is predominantly conducted using pseudo-homogenous models wherein the reactor environment is treated as a quasi-homogenous medium. Conceptually, such models neglect the essential role of topological non-uniformities and local flow maldistributions, and often are used with the assumptions of plug flow and equally distributed porosity throughout the bed. In spite of numerous experimental and analytical research efforts to incorporate the effects of local flow and structural non-uniformities into these models, e.g. (Giese et al., 1998; Kwapinski et al., 2004; Winterberg et al., 2000; Winterberg and Tsotsas,

2000a), even the most sophisticated models are still based upon lumped (effective) transport properties such as effective viscosity (Bey and Eigenberger, 2001; Kwapinski et al., 2004). The use of such effective transport properties leads to failure of even advanced versions of pseudo-homogenous models, such as the so-called $\Lambda_r(r)$ model which accounts for laterally uneven distributions of porosity, axial velocity and effective thermal conductivity (Winterberg et al., 2000; Winterberg and Tsotsas, 2000a), for accurate prediction of transport scalars at the pellet-scale in low-N fixed bed reactors. This failure can be attributed to the fact that when only a few pellets fit in a tube cross-section, azimuthal symmetry cannot be reasonably assumed (Dixon et al., 2006; Eppinger et al., 2011; Freund et al., 2005, 2003; Magnico, 2003; Nijemeisland and Dixon, 2004). Particle-resolved CFD simulations can offer a detailed insight into the role of spatial heterogeneity in the pellet-scale structure on the behavior of flow field and transport scalars (Dixon et al., 2012; Dong et al., 2017a; Singhal et al., 2017a). One of the pioneers in this direction were Derkx and Dixon (Derkx and Dixon, 1997), who conducted a 3D CFD simulation for a simple packed bed model with 3 spheres to obtain the wall heat

---

* Corresponding author.
  E-mail address: E.Moghaddam@Tudelft.nl (E.M. Moghaddam).

Nomenclature

d_o	the outer diameter of rings [m]	v_z	azimuthally-averaged axial velocity [m.s^{-1}]
d_i	the inner diameter of rings [m]	Δp	pressure drop [kg.m^{-1}s^{-2}]
d_{pv}	diameter of a sphere of equal volume [m]	r	radial Coordinate [m]
d_{ps}	diameter of a sphere of equal specific surface area [m]	z	axial Coordinate [m]
d_t	tube or bed diameter [m]		
h	height of pellet [m]	*Greek Letters*	
I	turbulence intensity [-]	ε	bulk porosity [-]
L	bed length [m]	$\varepsilon(r)$	radial porosity profile [-]
N	tube-to-pellet diameter ratio [-]	δ	thickness of Raschig ring [mm]
N_{pv}	tube-to-pellet diameter ratio based on d_{pv} [-]	μ	fluid dynamic viscosity [kg.m^{-1}s^{-1}]
N_{ps}	tube-to-pellet diameter ratio based on d_{ps} [-]	ρ	fluid phase density [kg.m^{-3}]
R_t	bed radius [m]	Ψ	dimensionless pressure drop introduced by Eq. (2) [-]
Re_p	Reynolds number based on d_{pv} =$\rho v_0 d_{pv}/\mu$ [-]		
v_o	inlet velocity [m.s^{-1}]		

---

transfer coefficient. Following this work, several research groups have used different finite volume- or finite element-based CFD codes to investigate the hydrodynamics and heat and mass transfer in surrogate models of tubular fixed bed reactors. Most CFD studies in the 2000s have been performed on small clusters of ordered packings of mainly spherical pellets or periodic wall segment models, which consist of a 120° slice of the bed cross-sectional area of a few layers of mostly spheres, see e.g. Dixon and coworkers (Dixon et al., 2008, 2006, 2005; Nijemeisland et al., 2004; Nijemeisland and Dixon, 2001; Taskin et al., 2008) and Guardo and coworkers (Coussirat et al., 2007; Guardo et al., 2007; 2005; 2004). Several research groups have also combined computer-generated random packings with particle-resolved CFD simulations of flow and transport scalars in tubular fixed beds (Atmakidis and Kenig, 2009; Bai et al., 2009; Boccardo et al., 2015; Dong et al., 2017a; Freund et al., 2005; Guo et al., 2019; Magnico, 2003). A detailed review on the noted approaches for modeling random packing structures was given by the present authors (Moghaddam et al., 2019). For instance, Magnico (2003) studied the influence of radial heterogeneities of the granular structures on the local flow and radial mass transfer in packed tubes of spheres with N = 5.96 and 7.8 at low to moderate particle Reynolds number, Re_p from 7 to 200. In a similar work, Freund et al. (2005) have used Lattice Boltzmann simulations to investigate the hydrodynamics and mass transfer in tubes with spheres with N = 5.96 at $Re_p \leq 100$. Similarly, Jafari et al. (2008), Atmakidis and Kenig (2009), Eppinger et al. (2011) and Robbins et al. (2012) have used computer-generated random packings of spheres in CFD studies of hydrodynamics for a wide range of Re_p. These studies have specifically focused on the influence of the wall on flow field and pressure drop in low-N packed beds of spheres. Basically, majority of the existing discrete-pellet CFD studies have addressed the problem of flow and heat transfer in spherical packing structures due to the simplicity of modelling the packing process for such a pellet shape (Augier et al., 2010; Behnam et al., 2013; Dixon et al., 2012; Eppinger et al., 2011; Singhal et al., 2017a). There are few publications addressing flow and heat transfer in packed beds with non-spherical particles (Boccardo et al., 2015; Partopour and Dixon, 2017; Singhal et al., 2017; Wehinger et al., 2015a, 2015b). This scarcity can be ascribed to inherent difficulties with handling collisions between non-spherical pellets (Lu et al., 2015; Moghaddam et al., 2018; Seelen et al., 2018; Zhong et al., 2016). The prevailing discrete-pellet CFD studies that account for non-spherical pellets in fixed beds can be classified into two main categories regarding the methodologies adopted to synthesize packing structures: (1) sequential Discrete Element Method (DEM)-CFD approach, and (2) sequential Rigid Body Dynamics (RBD)-CFD approach. The former category,

i.e. DEM-CFD, frequently uses the so-called glued-sphere or composite-sphere method (Lu et al., 2015), wherein the general framework of soft-sphere DEM is implemented to model shaped particles and their collisions during the loading process. Wehinger et al. (2015) have used the glued-sphere method to perform DEM-CFD simulations of flow, heat and reaction in packed tubes of spheres (d_p = 4 mm), cylinders (d_p/h = 5/5 mm) and Rashig rings ($d_o/d_i/h$ = 6.2/3.5/4.5 mm) with N = 3.6 at relatively low Re_p = 60. They investigated the influence of different pellet designs on the conversion and yield in dry reforming of methane. In another study, they dealt with the problem of contact point modification in discrete-pellet CFD simulation of heat transfer in random packing of cylinders with N = 4.04 and 191 < Re_p < 743 (Wehinger et al., 2017). Dong et al. (2017) investigated the radial heat transfer in a thin tube fixed bed stacked with glass spheres (d_p = 3 mm with 4 $\leq$ N<7) and steatite rings ($d_o/d_i/h$ = 6.2/3.5/4.5 mm with N = 3.4) for moderate flow conditions (60 < $Re_p \langle 1\ 0\ 0$) using the DEM-CFD method. The authors benchmarked their DEM-CFD results of heat transfer, e.g. the azimuthally-averaged temperature profile, against experimental data. Singhal et al. (2017b) have dealt with the problem of fluid-to-particle heat transfer using particle resolved direct numerical simulation (PR-DNS). The authors used Star CCM+ 11.02, a commercial DEM package, to generate packed beds of cylinders (d_p = 1 mm) with aspect ratio ranging from 2 to 6 using the glued-sphere method. Despite the promising outlook of DEM in handling non-spherical particles (Lu et al., 2015; Rakotonirina et al., 2018), the glued-sphere method, frequently used in DEM, depicted severe shortcomings, particularly in handling non-convex pellets (Lu et al., 2015; Zhong et al., 2016). For example, in the works of Wehinger et al. (2015) and Dong et al. (2017), the authors generated packing structures of Raschig rings by adding holes as a post-treatment to the final configuration of a DEM-generated packing of cylinders. This approach can only be accurate if the hole diameter is small enough such that the interpenetration between Raschig rings does not affect the bulk porosity of the generated structures.

There are a few studies that use sequential RBD-CFD to tackle flow and transport scalars in fixed beds of non-spherical particles. One of the pioneering works is the contribution of Boccardo et al. (2015), who used the open-source code Blender (a graphical software which uses the Bullet Physics Library) to synthesize packed beds of different pellet shapes such as spheres, cylinders, and tri-lobes. Similarly, Partopour and Dixon (2017) have developed a tailor-made integrated workflow using the Bullet Physics Library for computational generation of randomly packed beds of arbitrary-shaped pellets. The authors examined their automated package for the analysis of flow and pressure drop in random pack-

ings of spheres, cylinders, Raschig rings, and quadrilobes with five holes. Despite the existence of differences in the bulk porosity of sphere packings in cylindrical beds predicted by Blender compared to DigiDEM and LIGGGHTS, as reported by Fernengel et al. (2018), recently published results by Flaischlen and Wehinger (2019) demonstrate a better prediction of particle orientation in synthetically-generated packed columns of cylinders with Blender than Star-CCM+ software which uses the glued-sphere method to model non-spherical particles. The former authors underlined that further studies with incorporation of experimental analysis are needed in order to judge the accuracy of different collision methods as well as the impacts of approximations necessary to stabilize the simulations in the different approaches.

In our previous work (Moghaddam et al., 2019), we used our sequential RBD-CFD method (Moghaddam et al., 2018) to investigate packed beds with cylinders. This study addressed the importance of topological heterogeneity, inadequacy of azimuthal averaging, and the role of wall-effects on the velocity field and bed pressure drop. In this contribution, a similar study for Rashig rings, one of the most commonly-applied particle shapes in industry, is conducted. Here, tubular fixed beds containing Raschig rings with N = 3.06, 4.05 and 6.02 are considered. Surprisingly, literature information on Rashig rings is scarce, and available data only deals with individual case studies. Therefore, to the authors' knowledge, this is the first systematic numerical study of the porosity distribution and flow properties in relatively narrow beds with Rashig rings.

2. Methodology

2.1. RBD modeling of Raschig rings packing structures

The generation of 3D tubular beds packed with Raschig rings is carried out using our recently published RBD-based random packing algorithm, which employs a hard-body approach to handle collision phenomena. A detailed description together with a thorough validation is given in the original paper (Moghaddam et al., 2018). In the current work, a preset number of Raschig rings pellets are placed obliquely with an angle of 45° with respect to the gravity direction in a column in line with the tube axis, mimicking a sock loading scheme (see Moghaddam et al., 2018, for more details), and fall under the influence of gravity to the bottom of the tube. For each of these rings, a force-torque balance together with other auxiliary models accounting for pellet-pellet and (lateral and bottom) wall-pellet interactions, i.e. collisional contacts and resting contacts, are solved to simulate the random packing process. In our methodology, the transition between moving and resting particles, i.e. resting contact, is improved by a cutoff on sufficiently small relative contact velocities, instead of artificially damping translational and angular velocities during the entire filling process to stabilize the packing simulation. The RBD simulation stops when a dynamic equilibrium is reached. Since the resulting porosity of the RBD-simulated structures is highly influenced by the physiomechanical properties of pellets and container, tube-to-pellet diameter ratio and the loading method, we pursued the setup procedure reported in our previous work (Moghaddam et al., 2018) to synthesize the densest possible random packings of Raschig rings. Table 1 gives details of the preset parameters used for the RBD-based simulations. Fig. 1 illustrates the results of RBD-simulated packings of Raschig rings with different N.

2.2. Computational domain and mesh generation

For the mesh generation, details of the RBD-generated structures, i.e. the positions of the barycenters, the orientations and

Table 1
RBD simulation parameters.

Parameters	Preset Value
Pellet size [mm]	$d_o/d_i/h$ = 10/6/10
Number of face mesh per pellet [#]	8008
Pellet density [kg.m^{-3}]	8030
Tube size [mm]	d_t = 30.6, 40.5, 60.2; H = 150
Number of pellets used for initialization [#]	59, 125, 285, depending on d_t
Surface friction coefficient of pellets (dynamic)	0.1
Surface bounciness of pellets (COR*)	0.9
Surface friction coefficient of tube walls (dynamic)	0.6
Surface bounciness of tube wall (COR*)	0.6
Gravity acceleration [m s^{-2}]	9.81
Integration time step [s]	0.0025-0.025

* COR: Coefficient of Restitution.

Fig. 1. The RBD–simulated structures of Raschig rings with N_{pv} = 3.06, 4.05, 6.02.

the body face vertices of each Raschig ring, are imported to ANSYS Workbench 16.2 to reproduce a CAD model of the packing structure. A small interstice is then created between the pellets by shrinking each Raschig ring by 0.5% around its respective center of mass, which prevents highly skewed cells in the contact regions. The size of the created gap is small enough to have a negligible effect on the bulk porosity of the packing, and to prevent jet formation within the interstices even at high Re_p conditions (Dixon et al., 2013). The minor influence of this post-treatment on the bulk porosity of the structures is addressed quantitatively in Section 3.1. In this work, an advanced meshing approach, based on a combination of patch-independent and patch-conforming meshing methods, is implemented to creat an inflation mesh topology comprising of tetrahedral elements in the Raschig ring structures. This is conducted using an ad-hoc Python script in ANSYS Workbench 16.2. Further details of the meshing method together with the implementation of a graded meshing scheme in low-N packed columns, are presented in Moghaddam et al. (2019).

To achieve a precise prediction of the local velocity field in turbulent flow simulations, an appropriate mesh resolution is required, particularly in the contact regions. This was determined via a detailed mesh refinement study, in which the influence of different grid sizes (both min and max mesh sizes in a graded meshing scheme) and the number and thickness of prismatic layers on the resulted y^+ as well as local vector or scalar measurements, e.g. a vertex-averaged velocity along a line within the computational domain, was analyzed. We refer to our recent work

Table 2
Parameters used for mesh generation, and resulting mesh size for the RBD-simulated structures.

Meshing parameters	Values
max mesh size	$d_o/18.2$
min mesh size (=gap size)	$d_o/200$
growth rate in volume meshing	1.4 (including six inflation layers)
initial height for boundary-layer treatment	$2.5 \times 10^{-4} d_o$
number of layers for boundary-layer treatment	6
inflation rate used in boundary-layer treatment	1.2
thickness of boundary layer	$2.48 \times 10^{-3} d_o$

$N (d_t/d_o)$	Particle count in CFD Model (up to H = 100 mm)	Total number of cells ($\times 10^6$)
3.06	51	11.68
4.05	100	26.35
6.03	251	46.90

(Moghaddam et al., 2019), wherein a thorough mesh refinement analysis has been performed for resolved-particle CFD study of hydrodynamics in narrow-tube fixed beds of spheres and cylinders. According to our results, mesh independency can be appropriately reached with the values presented in Table 2, and thus we have implemented the same values in order to generate a graded mesh topology for the packing surrogates of Raschig rings. The final results of generated meshes, e.g. the total number of cells, are also given in Table 2. It is worth mentioning that the maximum mesh size employed is comparable to those used in most other similar studies (Atmakidis and Kenig, 2009; Behnam et al., 2013; Ding et al., 2005; Dixon et al., 2012; Eppinger et al., 2011; Taskin et al., 2008). Fig. 2 exhibits how the proposed inflation-layer meshing scheme results in finer cells at the contact regions. It is worth noting that the prism thickness layer chosen is fine enough to obtain the recommended dimensionless wall distance y^+ of approximately 1 according to the Enhanced Wall Treatment (EWT) approach.

2.3. CFD simulation setup

For the CFD simulations, the continuity and momentum equations are solved using the finite volume code ANSYS Fluent 16.2 for steady-state flow of an incompressible Newtonian fluid. The fluid phase is assumed to be isothermal with the standard physical properties of air (ρ = 1.225 kg/m^3, μ = 1.7894$\times 10^{-5}$ Pa.s). The air enters with a unidirectional and uniform velocity at the bottom of the system. This is introduced by a velocity-inlet boundary condition with the z-velocity component corresponding to the pellet Reynolds number, Re_p, ranging from 5 to 3.000, which is expressed by:

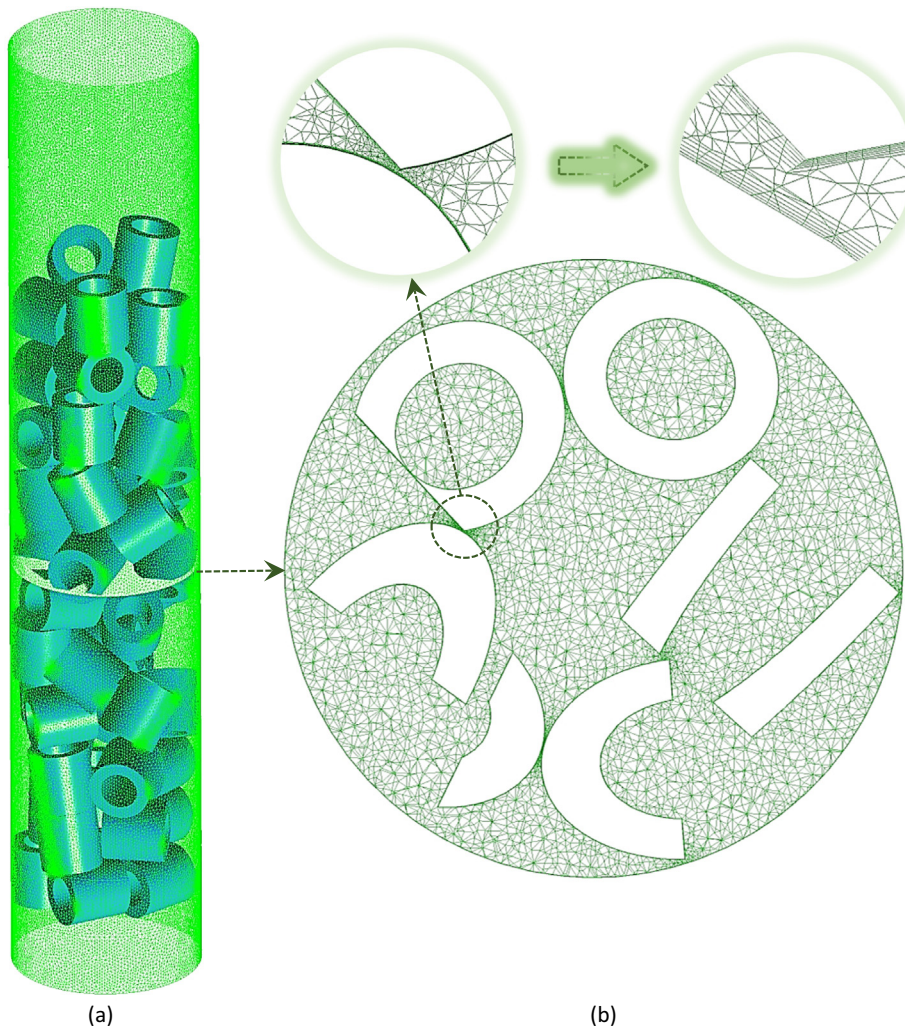(a)   (b)

Fig. 2. Graded mesh topology in random packing of Raschig rings with N = 3.06; (a) face mesh on the tube wall, (b) a cut plane of the volume mesh at height z = 7d$_p$.
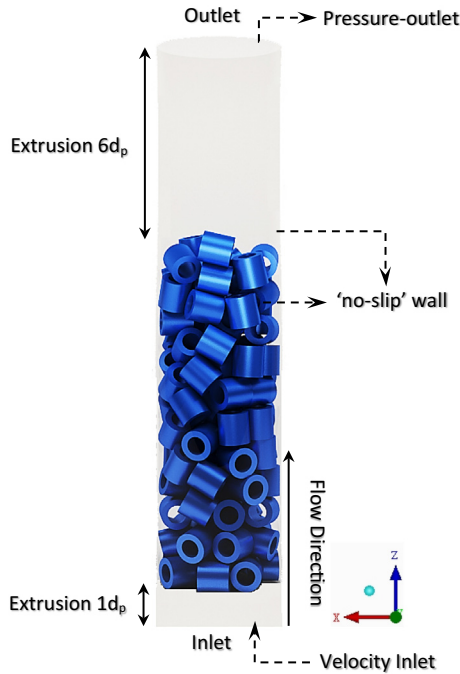
Fig. 3. Schematic overview of a packing model of Raschig rings and boundary conditions used in the CFD simulations; N = 4.05.

$$Re_p = \frac{\rho v_{0,z} d_{pv}}{\mu}$$

$$d_{pv} = \sqrt[3]{1.5h\left(d_o^2 - d_i^2\right)} \tag{1}$$

All solid surfaces, including the tube wall and the Raschig ring surfaces, are defined as 'no-slip' boundaries. The tube outlet boundary is set as a pressure-outlet condition with p = 1 bar. Furthermore, to minimize boundary effects, the bed entry and exit are extended by 1 and 6 pellet diameters, respectively. An overview of the flow model in conjunction with the preset boundary conditions are given in Fig. 3. The CFD simulations are performed in the laminar ($Re_p \leq 100$), transitional ($100 < Re_p < 600$) and turbulent ($Re_p \geq 600$) flow regimes, where the initial inlet turbulence intensity is computed based on the formula $I = 0.16\ Re^{-1/8}$ (where Re is based on the hydraulic diameter).

To simulate fully-turbulent flow, i.e. for $Re_p \geq 600$, the realizable k-ε model with an Enhanced-Wall-Treatment (EWT) is employed, which basically is a tried-and-tested RANS model for simulating flow fields with strong streamline curvature, see e.g. (Dixon et al., 2012; Dong et al., 2017a; Eppinger et al., 2011). It is worth mentioning that both the (laminar) Navier-Stokes equations and the realizable k-ε model have been examined for CFD simulations in the transitional flow regime.

3. Results and discussion

3.1. Bulk and local bed porosities

The RBD-generated packings of Raschig rings are characterized in terms of both global and radial porosity data. The bulk porosity of the simulated structures before and after bed shrinkage computed for the entire stack of Raschig rings up to the packing height of 120 mm (the calculation procedure is explained in Moghaddam et al. (2018), and then compared with literature data in Table 3. We note that the height of 120 mm corresponds to two packing layers from the upper part to minimize the effect of loose structures at the top part of the bed.

The results of the bulk porosity analysis demonstrate satisfactory agreement with the well-known empirical correlation proposed by Dixon (1988). Furthermore, the local shrinking of Raschig rings by 0.5% of their nominal diameter results in minor alterations to the bulk porosities of the packing structures, of the order of 0.7% to 1%, (see Table 3), which is reasonably small to not significantly affect the bed hydrodynamics. It is worth noting that the change in the computed bulk porosities of Raschig ring packings due to the local contraction of 0.5% is approximately half the change in bulk porosities for random packings of spheres and solid cylinders with the same N, reported in our previous study (Moghaddam et al., 2019).

Fig. 4 shows radial void fraction distribution obtained from the RBD-simulated structures versus wall distance, non-dimensionalized by the diameter of a volume-equivalent sphere. The results demonstrate influence of the tube wall on the ordering of the positions of Raschig rings along the tube radius. Such ordering has been addressed by many researchers for random packings of spheres and cylinders. However, as shown in Fig. 4, compared to the radial porosity profiles of solid cylinders, the profiles for Raschig rings are characterized by a series of humps, which originate from the axial holes in each pellet, repeating in a (damped-) oscillatory pattern towards the bed center. The position of the first peak in the vicinity of the tube wall is at the approximate distance of $0.5 d_{pv}$ from the container wall, which, comparing to the position of the first minimum in the radial void fraction profiles of full cylinders of the same outer diameter d_o, is a little shifted towards the tube wall. This may be attributed to the size of inner hole in such a pellet, as a higher hole-size would cause a higher change in the ordering of pellets at the near wall region compared with a full cylinder. Furthermore, the first hump starts at a distance of δ, extending over an approximate length of inner diameter d_i. The graphs also show that the gap distance between two neighbor humps is around 2δ. It is worth remarking that the local porosity at $(R_t-r)/d_{pv} = 1.5$ for random packing of Raschig rings with N = 3.06 increases to 1 (as shown in Fig. 3), which evidences the presence of a channel down the entire length of the tube. Such behavior has also been reported for packings of spheres and cylinders with N_{pv} around 4, (Behnam et al., 2013). The emergence of an axial channel in low-N packing structures is a consequence of restrictive

Table 3
Bulk porosity results of RBD-generated packings of Raschig rings.

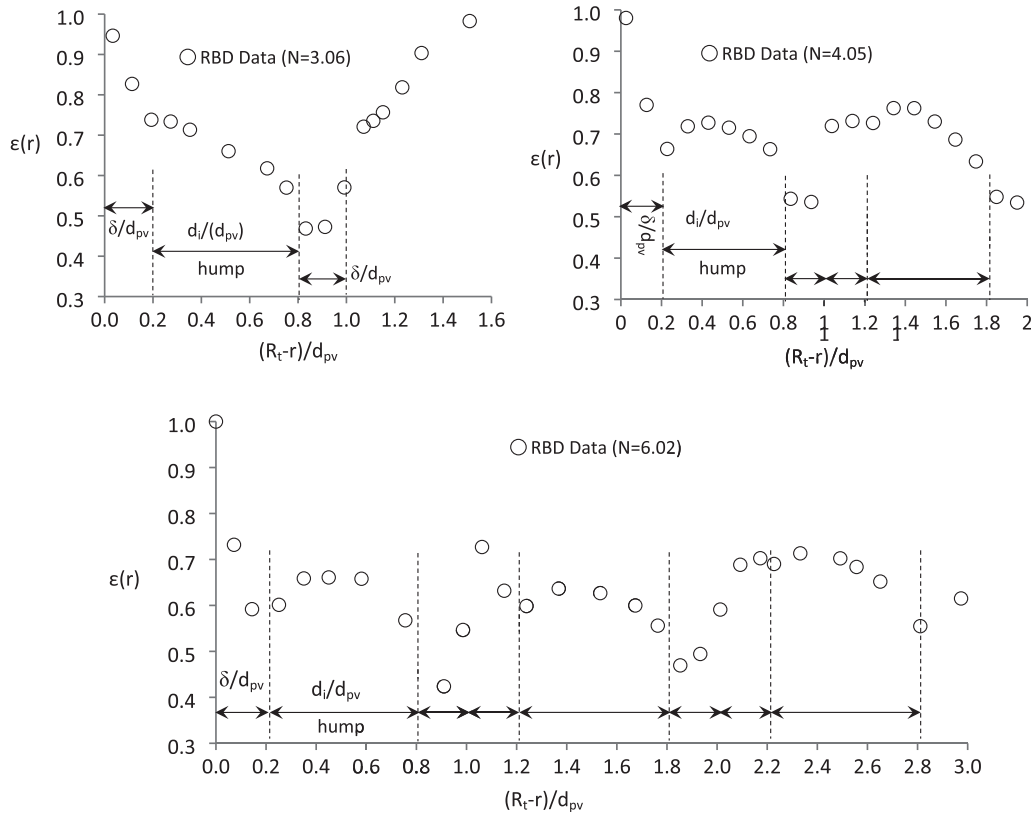| N (d_t/d_0)	N_{pv} (d_t/d_{pv})	Bulk porosity analysis (based on packing structure up to H = 120 mm)			
		Simulated (before shrinkage)	Dixon (1988)	MRE* (%)	Simulated (after shrinkage)
3.06	3.1	0.695	0.652	6.59	0.699
4.05	4.1	0.641	0.626	2.43	0.647
6.02	6.1	0.601	0.605	−0.77	0.607

*MRE: Mean Relative Error.

Fig. 4. Radial porosity profiles obtained from RBD-generated packings of Raschig rings (δ is the thickness of a Raschig ring).

structuring effects of the tube wall for such specific values of N, thereby preventing sliding of pellets towards the tube axis.

3.2. Pressure drop

To validate the CFD results, the computed bed pressure drops are benchmarked against the empirical correlation of Nemec and Levec (2005), applying the modifications proposed by Sonntag (1960), which account for the fraction of flow passing through the interior of a Raschig ring pellet. The resulting dimensionless pressure drop can be expressed as:

$$\Psi = \frac{\Delta P/L}{\rho g} = A \frac{Re_{ps}^*}{Ga^*} + B \frac{\left(Re_{ps}^*\right)^2}{Ga^*} \tag{2}$$

and

$$A = 150\mathfrak{R} \text{ and } B = 1.75\mathfrak{R} \tag{3}$$

$$\mathfrak{R} = \left[\frac{\varepsilon^3}{\left(1-(1-\varepsilon)(V_{fs}-mV_i)/V_p\right)^3}\right] \times \left[\frac{(S_f+mS_i)}{V_p}\frac{d_{ps}}{6}\right] \tag{4}$$

where V_{fc} and S_{fc} are the volume and surface of a full cylinder with the same outer diameter, d_o, and height, h, and V_i and S_i are the hole volume and surface area with an inner diameter of d_i. Here the fraction of an axial hole in the pellet available for flow (m) is approximated as 0.2, according to Sonntag (1960). Furthermore, Re_{ps}^* and Ga^* are the modified Reynolds number and the modified Galileo number, respectively, described by the following relationships:

$$Re_{ps}^* = \frac{\rho v_0 d_{ps}}{\mu(1-\varepsilon)} = \frac{6a Re_p}{d_p(1-\varepsilon)} \tag{5}$$

$$Ga^* = \left(\frac{\rho}{\mu}\right)^2 g\left(\frac{d_{ps}\varepsilon}{1-\varepsilon}\right)^3 \tag{6}$$

The CFD simulation results for the non-dimensional pressure drop, Ψ, computed based on a bed height of 0.1 m (including 10 layers of Raschig rings) are plotted against the empirical correlations by Nemec and Levec (2005) and Ergun (1952) in Fig. 5. The results show satisfactory agreement between the CFD data and the correlation of Nemec and Levec (2005), in all flow regimes, particularly for packed columns of Raschig rings with N = 4.05 and 6.02, leading to mean relative errors (MRE%) of 14.8% and 17.8%, respectively. It is noteworthy that the Ergun equation, even if it is improved by the equivalent particle diameter, i.e. d_{ps}, to cater for the effect of the pellet's shape, underestimates the pressure drop in packed beds of Raschig rings with mean relative errors of 67.5% and 75.2% for packings with N = 4.05 and 6.02, respectively. In fact, the interior of rings acts as an additional source for eddy formation as well as dead spaces inside the bed (see Figs. 8 and 9) compared to spheres. The influence of such a feature cannot be counterbalanced with a higher specific surface area of rings and accordingly lower d_{ps}, leading to a higher pressure drop in such structures than originally predicted by the Ergun equation (see Fig. 5).

However, for the packing structure with N = 3.06, the MRE% calculated based on both correlations is around 28% (deviations from Nemec and Levec and Ergun equations are calculated as 28.3% and 28.9%, respectively). The lower deviation for the Ergun equation, found for this case, can be explained by the lower computed pressure drop due to the presence of an axial channel in the center of the packing with N = 3.06 (as highlighted in Section 3.1).

3.3. Structure of flow fields

The in-situ behavior of the flow field in random packing structures has been the topic of numerous experimental and analytical studies during the last two decades (Bai et al., 2009; Baker et al., 2011; Bey and Eigenberger, 1997; Boccardo et al., 2015; Freund
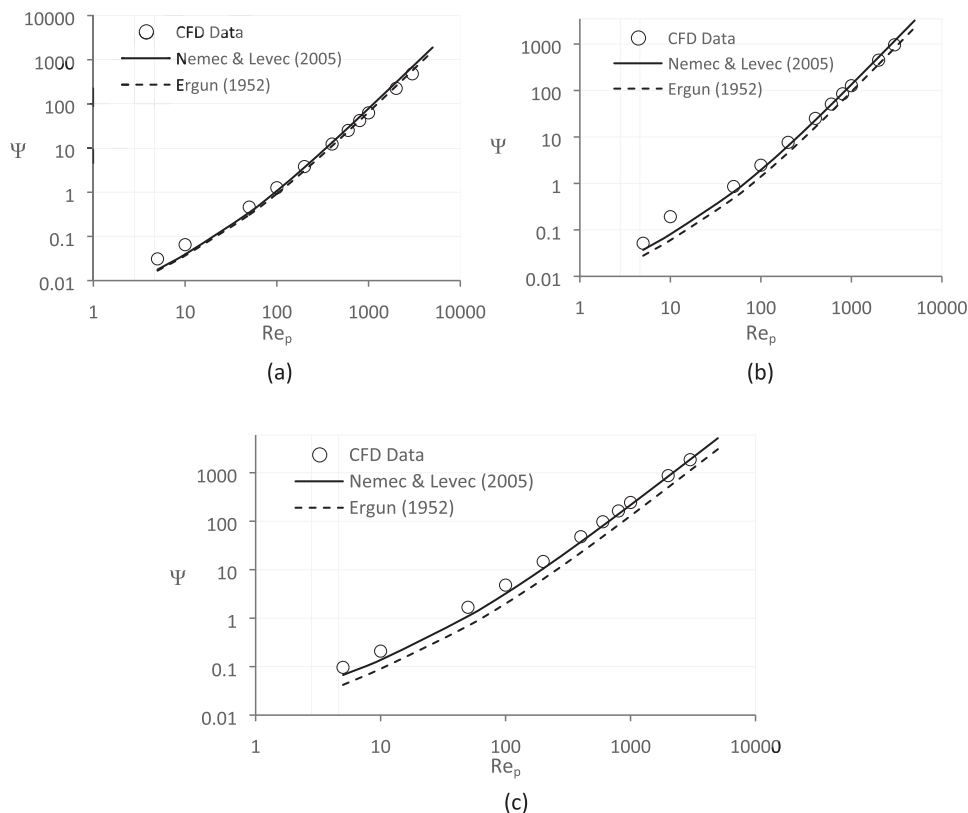
Fig. 5. Comparison between the dimensionless pressure drops obtained from RBD-CFD simulations and empirical correlations for packings of Raschig rings with: (a) N = 3.06, (b) N = 4.05 and (c) N = 6.02.

et al., 2003; Giese et al., 1998; Wehinger et al., 2017), as it has a crucial effect on local propagation of transport scalars inside the reactor, and, accordingly, on the reactor performance. However, as addressed in the introduction, only few studies deal with the flow structure inside a random packing of Raschig rings. In Fig. 6, two examples of the contour plots of axial velocity, normalized by the inlet velocity, together with flow streamlines colored by the axial velocity are illustrated for packed columns of Raschig rings with N = 3. 4.04 and 6.02 at a typical $Re_p = 00$.

The contour plots of normalized axial velocity show significant inhomogeneity, both in the azimuthal (θ-) direction at each cross-section and along the packing height. Furthermore, the contour plots at each cross section show the significance of Raschig ring orientation because the rings situated in parallel with the flow direction can tremendously increase the local velocity through their interiors.

Overall, the contour map reveals a local increase of axial velocity up to factors of 5.81, 7.83 and 10.6 for packings of Raschig rings with N_{pv} = 3.1, 4.1 and 6.1, respectively, at Re_p = 100. The local rise in axial velocity increases with N at each specific Re_p (as evidenced by the above-mentioned statistics for the maximum v_z/v_0 found in packings with different N_{pv}), which can be explained by the decrease of the bulk porosity with increasing N. Similar results are found for the magnitude of negative z-velocity (e.g. v_z/v_0 = -1.08, -1.76 and -3.58 for N = 3.06, 4.05 and 6.02, respectively).

When comparing these results with our previous study on low-N fixed beds with spheres and cylinders (Moghaddam et al., 2019), it is found that the highest local increase of axial velocity occurs in packings of cylinders, then spheres and then Raschig rings for similar N_{pv} and Re_p. For example, maximum v_z/v_0 values are 7.72, 7.24 and 5.81, respectively, for packings of cylinders, spheres and rings with N_{pv} = 3.1 at Re_p = 100, and maximum v_z/v_0 values are 12.02,

8.58 and 7.83, respectively, for packings of cylinders, spheres and rings with N_{pv} = 4.1 at Re_p = 100. The relatively lower local maxima can be attributed to the shape of Raschig rings pellets, where the existence of an axial hole inside such pellets increases the local porosity. It is worth remarking that, contrary to the random packings of spheres and cylinders wherein the high velocity fields are found predominantly near the wall region (Dong et al., 2017a; Eppinger et al., 2011; Moghaddam et al., 2019; Wehinger et al., 2017), high velocity hotspots appear throughout the tube cross-section for Raschig ring packings, particularly at the interior part of pellets situated parallel to the flow direction. Furthermore, areas with backflow appear inside the pellets located perpendicular to the flow direction. These phenomena can be more clearly viewed via the contours of axial velocity at the central plane (XZ plane) of the packings, as shown in Fig. 7.

As illustrated in Fig. 7a, maximum axial velocities occur at the center of the packing geometry with N around 3, which stems from a high local porosity near the tube center in such packing structures. This circumstance can also be inferred from the radial porosity profile of this packing structure, as shown in Fig. 4. Several researchers have also reported similar observations for packings of spheres with N_{pv} around 4 (Behnam et al., 2013; Eppinger et al., 2011; Freund et al., 2003; Moghaddam et al., 2019), and also for cylinders with N slightly larger than 4 (Moghaddam et al., 2019). Furthermore, the contour plots reveal that areas with stagnant and backflow velocity fields are not only emerging in the wakes of pellets, as observed for spheres and cylinders (Eppinger et al., 2011; Moghaddam et al., 2019), but are mostly appearing inside the rings situated perpendicular to the flow direction.

Fig. 8 highlights all fluid cells with stagnant and backflow fields in a random packing of Raschig rings with N = 4.05 at different Re_p. As Fig. 8 shows, the volume fraction of such regions increases with
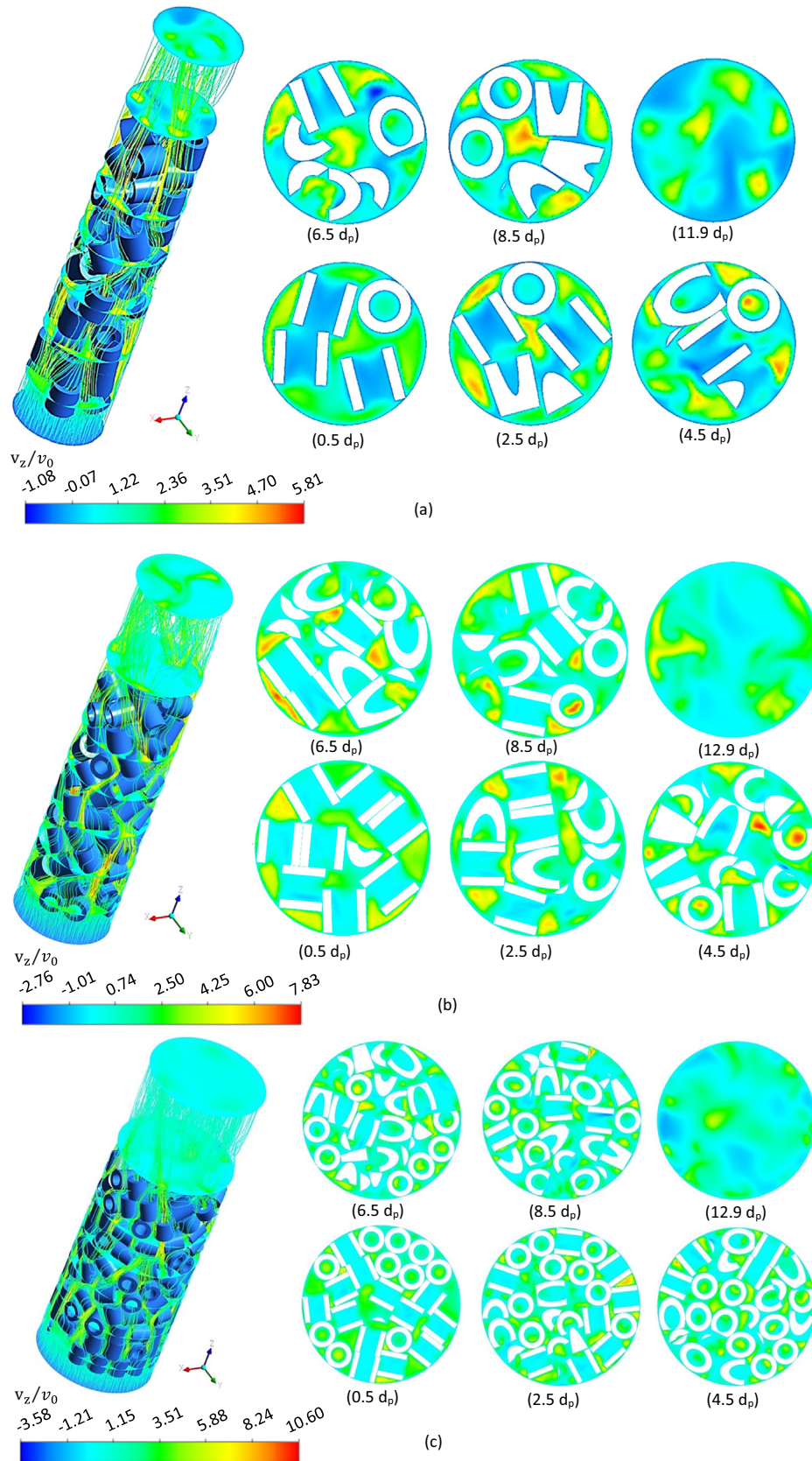
Fig. 6. Examples of 3D flow fields using streamlines and contour plots of normalized axial velocity at different cross sections at axial positions 0.5d$_p$, 2.5d$_p$, 4.5d$_p$, 6.5d$_p$, 8.5d$_p$ and +0.5d$_p$ behind the packing section, for packings of Raschig rings, with: (a) N = 3.06, (b) N = 4.03 and (b) N = 6.02 at Re$_p$ = 100.
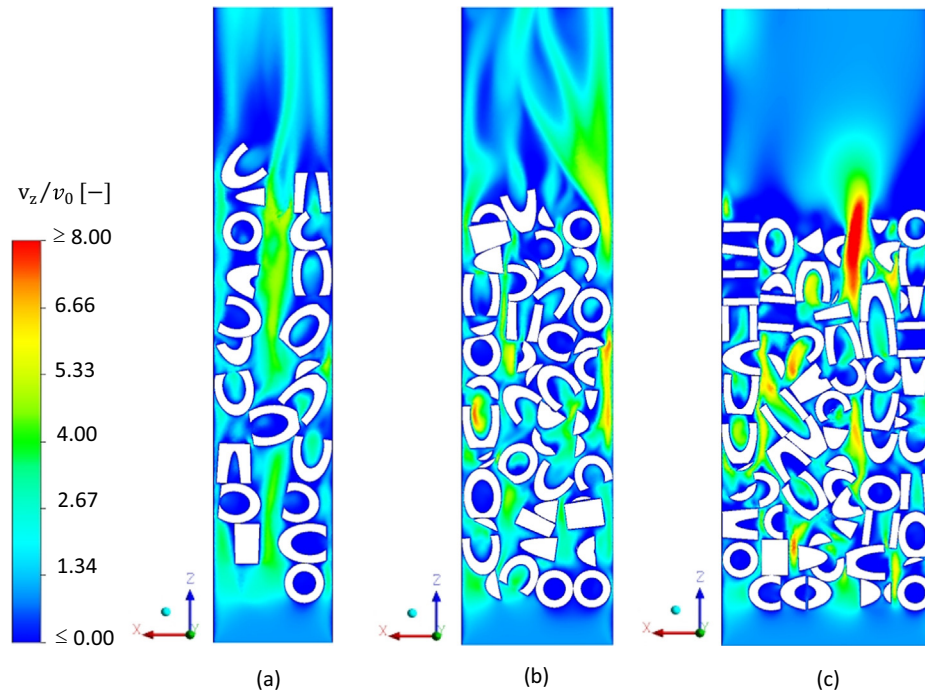
Fig. 7. Contour plots of normalized axial velocity at the central plane (XZ) of packings with: (a) N = 3.06, (b) N = 4.05 and (c) N = 6.02 at Re_p = 100.
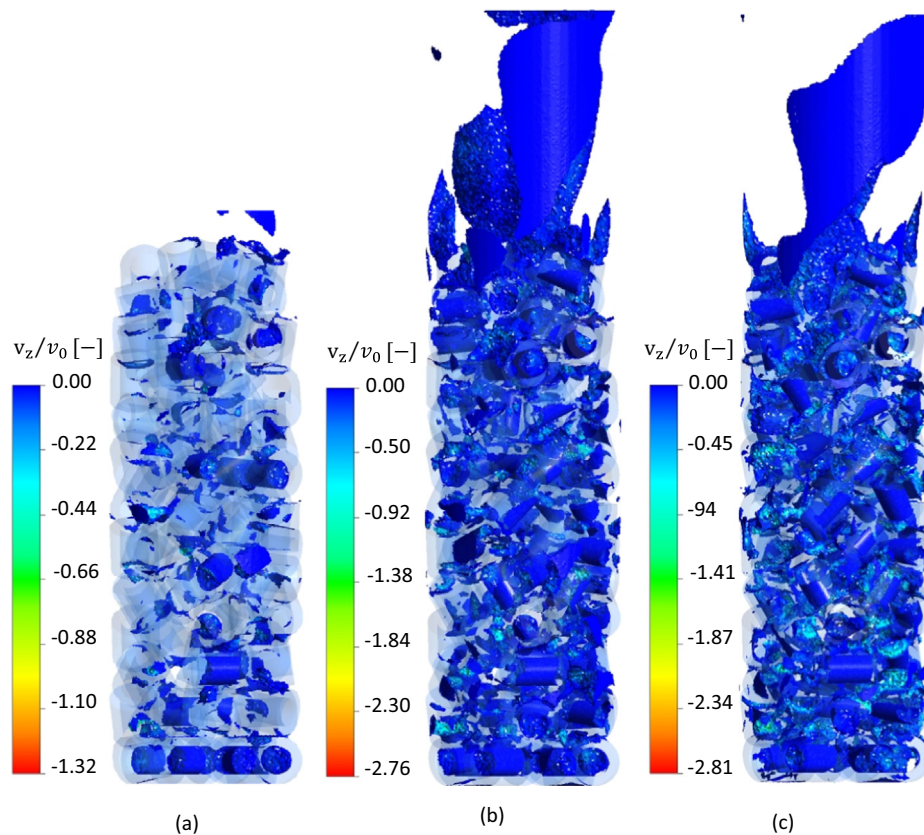

Fig. 8. Regions with stagnant and backflow velocity fields in a random packing of Raschig rings with N = 4.05; a) Re_p = 10, b) Re_p = 100 and c) Re_p = 1000.

increasing Re_p, which implies the crucial role of eddy transport at higher flow conditions in fixed bed systems.

In Fig. 9, the volume fraction of fluid cells with stagnant and backflow velocity fields are compared for random packings of spheres, cylinders (these results were extracted from the results of our previous CFD study on spheres and cylinders, Moghaddam et al., 2019) and Raschig rings with N_{pv} = 4.1 at different Re_p values. The results demonstrate a higher volume fraction of backflow
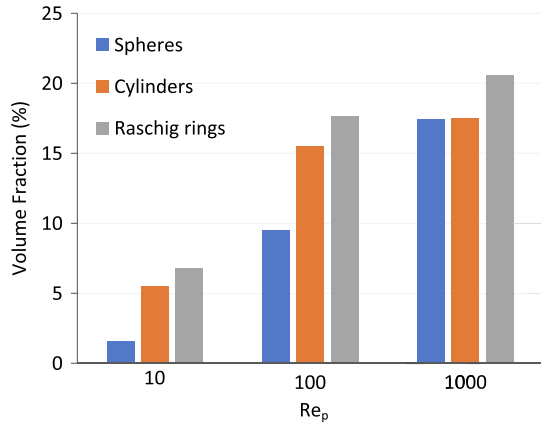
Fig. 9. Volume fractions of fluid cells with stagnant and backflow velocity fields in random packings of spheres, cylinders and Raschig rings with $N_{pv} \sim 4.1$ for a packing height of 0.1 m at different Re_p.

regions in a fixed bed of Raschig rings compared to spheres and cylinders with the same N_{pv}, which arises from the presence of a hole inside each pellet, providing additional space for formation of vortices. Such a characteristic behavior offers a higher residence time, as well as a better local mixing in the fluid phase, which altogether can enhance the transport rate at the pellet scale in fixed beds of Raschig rings.

3.4. Azimuthally-averaged velocity profiles

During the last two decades, several research groups have strived to modify the earlier classical pseudo-homogenous plug flow models by introducing the velocity field in the form of a radially varying axial velocity, $v_z(r)$ (Bey and Eigenberger, 2001; Dixon et al., 2006; Winterberg and Tsotsas, 2000b). Such a velocity field can be obtained from a modified momentum balance or a form of Brinkman-Forcheimer-extended Darcy (BFD) equation (Bey and Eigenberger, 2001 & 1997; Giese et al., 1998). Comparisons are made based on this modification and good agreement obtained, provided that an adjustable effective viscosity is introduced into the term catering for wall effects, which depends on Re_p, pellet shape, the assumed pressure drop correlation, and the porosity in the near-wall region (Subagyo et al., 1998; Winterberg et al., 2000; Winterberg and Tsotsas, 2000). The axial velocity profile in the form of $v_z(r)$ can also be obtained from CFD results by azimuthal averaging of the 3D velocity field at different bed cross sections. For instance, Fig. 10 illustrates the azimuthally-averaged axial velocity distributions obtained from two different packing depths and the axially-and-azimuthally-averaged profile together with the radial porosity data for all packing models at $Re_p = 1000$.

As shown in Fig. 10, the first maximum of the azimuthally-averaged axial velocities occurs adjacent to the tube wall and varies between 1.5 and 3 times the inlet superficial velocity, which corresponds to the values obtained by Bey and Eigenberger (1997) and Giese et al. (1998). Furthermore, Fig. 10a shows a tremendous increase of averaged axial velocities at the bed center, which is attributed to the presence of a channel along the tube axis in Raschig ring packing with N = 3.06. The figure also demonstrates that the first minimum of the global (axially-and-azimuthally-averaged) axial velocity profile takes place at approximately $0.85d_{pv}$ from the tube wall, corresponding to the first minimum in the local porosity profile, i.e. at the end of the first hump region. Compared to the position of the first minima in global axial velocity profiles for fixed beds of spheres and cylinders, which occur approximately at $0.5d_{pv}$ and $0.65d_{pv}$ from the tube wall (Behnam et al., 2013;
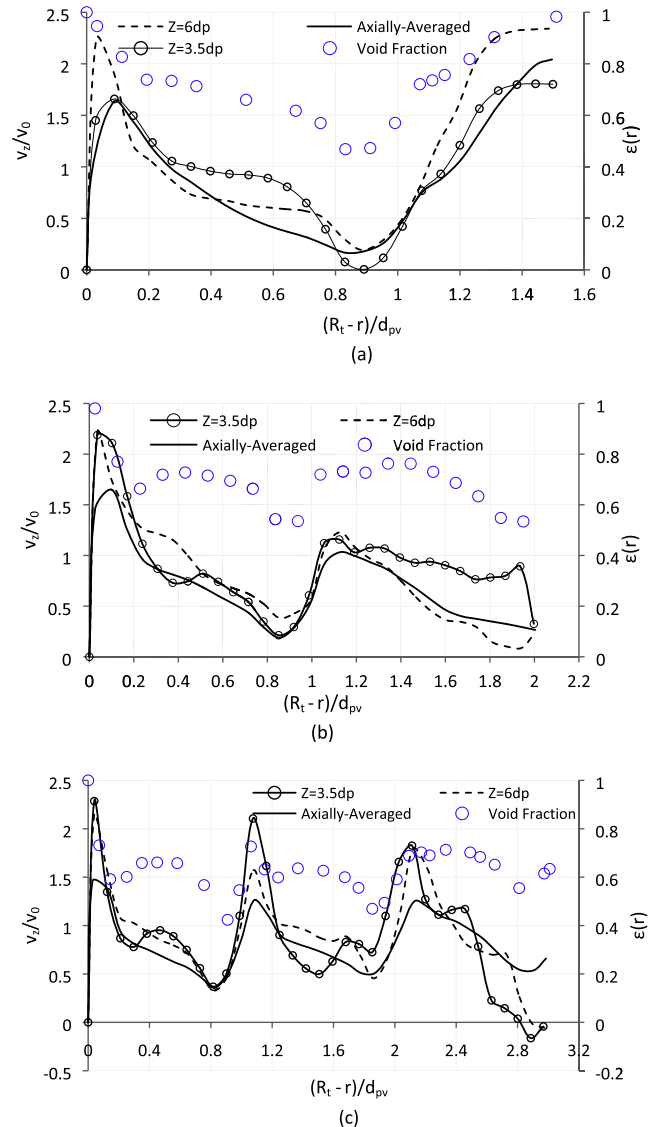

Fig. 10. Azimuthally–averaged axial velocity profiles at cross-sections $z = 3.5d_p$, $6d_p$ and axially-azimuthally-averaged profile at $Re_p = 1000$ together with the radial void fraction data for packings of Raschig rings with: (a) N = 3.06, (b) N = 4.04 and (c) N = 6.02.

Eppinger et al., 2011; Freund et al., 2003; Moghaddam et al., 2019; Wehinger et al., 2017), this position shifts a little towards the bed center region for packings of Raschig rings. This may result in a smoother trend of lateral dispersion of transport scalars in such a packing structure. Nonetheless, a distinct difference between the local (azimuthally-averaged) and the global (axially-and-azimuthally-averaged) v_z/v_0 profiles can be observed, particularly at the points where the local porosity has its extreme values. Our results show that local deviations are stronger in narrower structures, e.g. N = 3.06, where azimuthal symmetry basically cannot be assumed, resulting in large inhomogeneity in $v_z(r)$ along the bed axis. For instance, Fig. 10a reveals that local azimuthally-averaged z-velocity at $z = 6d_p$, i.e. $v_z(r,z = 6d_p)$, deviates up to 129% (with an average deviation of 27%) from the global (axially-and-azimuthally averaged) velocity $v_z(r)$ for a packing of Raschig rings with N = 3.05 at $Re_p = 1000$. Similarly, Fig. 10b & c show deviations of up to 76% (with an average deviation of 17%) and up to 68% (with an average deviation of 21%) for packings of Raschig rings with N = 4.06 and 6.02 at $Re_p = 1000$, respectively.

Overall, despite the fact that the results demonstrate an oscillatory pattern of the axially-and-azimuthally averaged axial velocity profile along bed radius, contrary to the spherical and cylindrical cases (Atmakidis and Kenig, 2009; Eppinger et al., 2011; Moghaddam et al., 2019), it is hard to find a meaningful correlation between the global axial velocity profiles and the radial porosity distribution in random packings of Raschig rings.

The axially-and-azimuthally-averaged axial velocity profiles (solid lines) are compared with the azimuthally-averaged (dashed lines) and the in-situ axial velocity data (blue circles) in Fig. 11 at a typical cross section, $z = 6d_p$, in Raschig rings packings with N = 3.06 and 4.05 at $Re_p = 1000$.

Overall, the results show a very high deviation of more than 500% of the (axially-and-) azimuthally-averaged values of axial velocities, even if obtained for a specific bed cross section, e.g. $z = 6d_p$, from the local axial velocity values. Furthermore, Fig. 11 demonstrates that the maximum deviations (a local increase of up to $13v_0$ with respect to the azimuthally-averaged axial velocity profile) occur approximately at the position of the first minimum in the axially-and-azimuthally-

averaged axial velocity profile, i.e. at the approximate distance of $0.85d_{pv}$ from the tube wall, which also corresponds to the position of the first minimum in the radial porosity profile. A remarkable difference between the local and azimuthally-averaged values of v_z/v_0 can be observed in the vicinity of the tube wall. Such noticeable deviations can result in erroneous predictions of the apparent wall Nusselt number as $Nu_w \propto Re_p^{0.7}$ and, accordingly, in the transverse wall heat flux, which can lead to an erroneous prediction of the temperature field in a highly endothermic or exothermic reactions with very sharp temperature gradients (where low-N tubular fixed beds are often used). The influence of azimuthal averaging of 3D velocity field on the deviation of predicted radial temperature profile from 3D temperature field inside low-N tubular fixed beds will be investigated quantitatively in our forthcoming paper. Furthermore, as illustrated in Fig. 11, the azimuthally-averaged axial velocities are generally positive, while the actual local velocities can be negative, which substantiates the inadequacy of such averaged velocity field information in reflecting the appearance of vortex regions, i.e. backflow as well as stagnant flow fields.
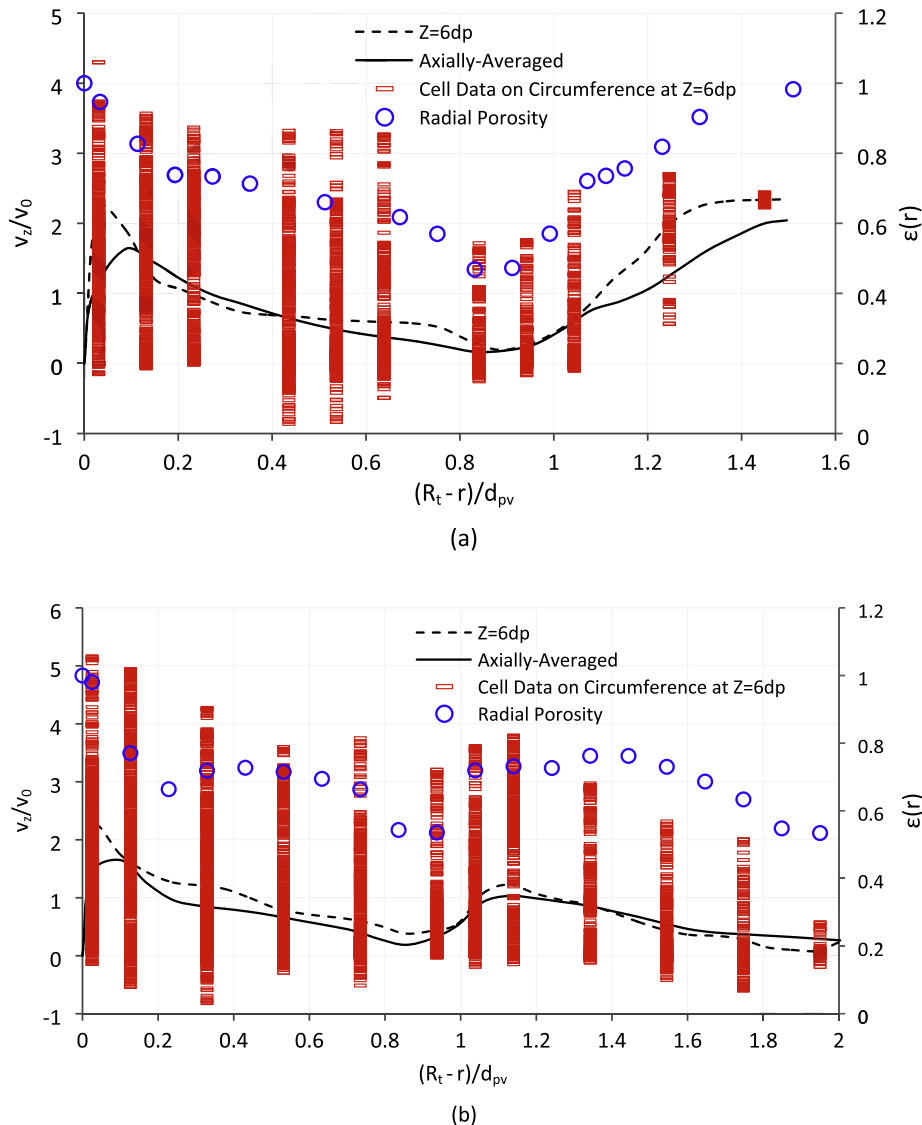

Fig. 11. Axially-and-azimuthally–averaged axial velocity profiles (solid lines) compared with the azimuthally-averaged axial velocity profiles (dashed lines) and in-situ axial porosity data extracted at different positions (blue circles) at the cross-section $z = 6d_p$ for Raschig ring packings with: (a) N = 3.06 and (b) N = 4.05, at $Re_p = 1000$.

4. Conclusions

Discrete-pellet CFD simulations of flow field and pressure drop in fixed beds of Raschig rings were conducted for a wide range of Re$_p$ values. For this, a tailor-made integrated workflow is employed (Moghaddam et al., 2019), which is based on the sequential generation of the packing structures containing non-spherical pellets by means of our RBD-based random packing algorithm (Moghaddam et al., 2018), and the hydrodynamics using relevant CFD concepts. Overall, the methodology offers substantial improvements over the DEM-CFD approach in which a glued-sphere method is often applied to synthesize random packings of non-convex pellets.

The CFD results have been validated by comparing the computed pressure drop to published empirical correlations. It is demonstrated that even an improved Ergun equation, which is modified by the equivalent particle diameter, d$_{ps}$, to account for the role of the pellet's non-sphericity, underestimates the pressure drop in fixed beds of Raschig rings significantly, e.g. leading to a mean relative deviation of 75.2% for the packed column with N = 6.02 for the investigated range 5 < Re$_p$ < 3000. The reason for this deviation, as established here, is due to the contribution of additional sources of vortex regions: the axial hole in Raschig rings in effect provides an additional source for backflow fields inside a bed. The total pressure drop cannot be counterbalanced by a higher specific surface area of the rings, which results in a higher pressure drop in such structures than originally predicted by the modified Ergun equation.

The 3D structures of the flow fields demonstrate a large influence of local topology on the velocity distribution at the pellet scale. The contour plots of the axial velocity at different cross-sections reveal: (i) a remarkable inhomogeneity both in the azimuthal direction at each cross section and along the packing height, which directly stems from a strong spatial heterogeneity in such complicated topologies, and (ii) a significant influence of Raschig ring orientation in the packing topology on local flow field, as the rings oriented in line with the flow direction can tremendously accelerate the local velocity through their axial holes, while those oriented perpendicular to the flow direction provide additional sources for eddy formation.

The CFD results also show that azimuthal-averaging of the 3D velocity field along the packing structure not only cannot reflect the areas with backflow field and vortex regions, but also leads to an error in the local velocity values of more than 500% of the inlet superficial velocity. This might explain the inadequacy of even modified versions of pseudo-continuum approaches, wherein the global azimuthally-averaged axial velocity profile is contributed to account for the role of velocity field, in predicting the local transport scalars inside such low-N fixed bed reactors. Of course, it is possible that transport scalars such as temperature and concentration may not respond to structural inhomogeneity as strongly as the velocity field. This will be the topic of our next work.

CRediT authorship contribution statement

E.M. Moghaddam: Conceptualization, Methodology, Software, Validation, Writing-original draft, Visualization, Funding acquisition. **E.A. Foumeny:** Supervision, Writing-review & editing. **A.I. Stankiewicz:** Supervision, Resources, Project administration, Funding acquisition. **J.T. Padding:** Supervision, Conceptualization, Resources, Writing-review & editing, Funding acquisition.

Declaration of Competing Interest

The authors declare that they have no known competing financial interests or personal relationships that could have appeared to influence the work reported in this paper.

References

Atmakidis, T., Kenig, E.Y., 2009. CFD-based analysis of the wall effect on the pressure drop in packed beds with moderate tube/particle diameter ratios in the laminar flow regime. Chem. Eng. J. 155, 404–410. https://doi.org/10.1016/j.cej.2009.07.057.

Augier, F., Idoux, F., Delenne, J.Y., 2010. Numerical simulations of transfer and transport properties inside packed beds of spherical particles. Chem. Eng. Sci. 65, 1055–1064. https://doi.org/10.1016/j.ces.2009.09.059.

Bai, H., Theuerkauf, J., Gillis, P.A., Witt, P.M., 2009. A coupled DEM and CFD simulation of flow field and pressure drop in fixed bed reactor with randomly packed catalyst particles. Ind. Eng. Chem. Res. 48, 4060–4074.

Baker, M.J., Young, P.G., Tabor, G.R., 2011. Image based meshing of packed beds of cylinders at low aspect ratios using 3d MRI coupled with computational fluid dynamics. Comput. Chem. Eng. 35, 1969–1977. https://doi.org/10.1016/j.compchemeng.2011.03.017.

Behnam, M., Dixon, A.G., Nijemeisland, M., Stitt, E.H., 2013. A new approach to fixed bed radial heat transfer modeling using velocity fields from computational fluid dynamics simulations. Ind. Eng. Chem. Res. 52, 15244–15261. https://doi.org/10.1021/ie4000568.

Bey, O., Eigenberger, G., 2001. Gas flow and heat transfer through catalyst filled tubes. Int. J. Therm. Sci. 40, 152–164. https://doi.org/10.1016/S1290-0729(00)01204-7.

Bey, O., Eigenberger, G., 1997. Fluid flow through catalyst filled tubes 52.

Boccardo, G., Augier, F., Haroun, Y., Ferre, D., Marchisio, D.L., 2015. Validation of a novel open-source work-flow for the simulation of packed-bed reactors. Chem. Eng. J. 279, 809–820. https://doi.org/10.1016/j.cej.2015.05.032.

Coussirat, M., Guardo, A., Mateos, B., Egusquiza, E., 2007. Performance of stress-transport models in the prediction of particle-to-fluid heat transfer in packed beds. Chem. Eng. Sci. 62, 6897–6907. https://doi.org/10.1016/j.ces.2007.08.071.

Derkx, O.R., Dixon, A.G., 1997. Effect of the wall Nusselt number on the simulation of catalytic fixed bed reactors. Catal. Today 35, 435–442. https://doi.org/10.1016/S0920-5861(96)00210-6.

Ding, Y., Wang, Z., Wen, D., Ghadiri, M., Fan, X., Parker, D., 2005. Solids behaviour in a gas – solid two-phase mixture flowing through a packed particle bed. Chem. Eng. Res. Des. 60, 5231–5239. https://doi.org/10.1016/j.ces.2005.04.052.

Dixon, A.G., 1988. Correlations for wall and particle shape effects on fixed bed bulk voidage. Can. J. Chem. Eng. 66, 705–708. https://doi.org/10.1002/cjce.5450660501.

Dixon, A.G., Ertan Taskin, M., Nijemeisland, M., Stitt, E.H., 2008. Wall-to-particle heat transfer in steam reformer tubes: CFD comparison of catalyst particles. Chem. Eng. Sci. 63, 2219–2224. https://doi.org/10.1016/j.ces.2008.01.017.

Dixon, A.G., Nijemeisland, M., Stitt, E.H., 2013. Systematic mesh development for 3D CFD simulation of fixed beds: contact points study. Comput. Chem. Eng. 48, 135–153. https://doi.org/10.1016/j.compchemeng.2012.08.011.

Dixon, A.G., Nijemeisland, M., Stitt, E.H., 2006. Packed tubular reactor modeling and catalyst design using computational fluid dynamics. Adv. Chem. Eng. 31, 307–389. https://doi.org/10.1016/S0065-2377(06)31005-8.

Dixon, A.G., Nijemeisland, M., Stitt, E.H., 2005. CFD study of heat transfer near and at the wall of a fixed bed reactor tube : effect of wall conduction. Ind Eng. Chem. Res. 44, 6342–6353.

Dixon, A.G., Walls, G., Stanness, H., Nijemeisland, M., Stitt, E.H., 2012. Experimental validation of high Reynolds number CFD simulations of heat transfer in a pilot-scale fixed bed tube. Chem. Eng. J. 200–202, 344–356. https://doi.org/10.1016/j.cej.2012.06.065.

Dong, Y., Sosna, B., Korup, O., Rosowski, F., Horn, R., 2017. Investigation of radial heat transfer in a fixed-bed reactor: CFD simulations and profile measurements. Chem. Eng. J. 317, 204–214. https://doi.org/10.1016/j.cej.2017.02.063.

Eppinger, T., Seidler, K., Kraume, M., 2011. DEM-CFD simulations of fixed bed reactors with small tube to particle diameter ratios. Chem. Eng. J. 166, 324–331. https://doi.org/10.1016/j.cej.2010.10.053.

Ergun, S., 1952. Fluid flow through packed columns. Chem. Eng. Prog. 48, 89–94.

Fernengel, J., von Seckendorff, J., Hinrichsen, O., 2018. Influence of cylinder-to-particle diameter ratio and filling speed on bed porosity of random packed beds of spheres. Computer Aid. Chem. Eng. Elsevier Masson SAS, 97–102. https://doi.org/10.1016/B978-0-444-64235-6.50019-X.

Flaischlen, S., Wehinger, G.D., 2019. Synthetic packed-bed generation for CFD simulations: blender vs STAR-CCM+. Chem. Eng. 3 (52). https://doi.org/10.3390/chemengineering3020052.

Freund, H., Bauer, J., Zeiser, T., Emig, G., 2005. Detailed simulation of transport processes in fixed-beds. Ind. Eng. Chem. Res. 44, 6423–6434. https://doi.org/10.1021/ie0489453.

Freund, H., Zeiser, T., Huber, F., Klemm, E., Brenner, G., Durst, F., Emig, G., 2003. Numerical simulations of single phase reacting flows in randomly packed fixed-bed reactors and experimental validation. Chem. Eng. Sci. 58, 903–910. https://doi.org/10.1016/S0009-2509(02)00622-X.

Giese, M., Rottschafer, K., Vortmeyer, D., 1998. Measured and modeled superficial flow profiles in packed beds with liquid flow. AIChE J. 44, 484–490. https://doi.org/10.1002/aic.690440225.

Guardo, A., Coussirat, M., Larrayoz, M.A., Recasens, F., Egusquiza, E., 2005. Influence of the turbulence model in CFD modeling of wall-to-fluid heat transfer in packed beds. Chem. Eng. Sci. 60, 1733–1742. https://doi.org/10.1016/j.ces.2004.10.034.

Guardo, A., Coussirat, M., Larrayoz, M.A., Recasens, F., Egusquiza, E., 2004. CFD flow and heat transfer in nonregular packings for fixed bed equipment design. Ind. Eng. Chem. Res. 43, 7049–7056.

Guardo, A., Coussirat, M., Recasens, F., Larrayoz, M.A., Escaler, X., 2007. CFD studies on particle-to-fluid mass and heat transfer in packed beds: Free convection effects in supercritical fluids. Chem. Eng. Sci. 62, 5503–5511. https://doi.org/10.1016/j.ces.2007.02.040.

Guo, Z., Sun, Z., Zhang, N., Ding, M., Zhou, Y., 2019. Influence of flow guiding conduit on pressure drop and convective heat transfer in packed beds. Int. J. Heat Mass Transf. 134, 489–502. https://doi.org/10.1016/j.ijheatmasstransfer.2019.01.066.

Jafari, A., Zamankhan, P., Mousavi, S.M., Pietarinen, K., 2008. Modeling and CFD simulation of flow behavior and dispersivity through randomly packed bed reactors. Chem. Eng. J. 144, 476–482. https://doi.org/10.1016/j.cej.2008.07.033.

Kwapinski, W., Winterberg, M., Tsotsas, E., Mewes, D., 2004. Modeling of the wall effect in packed bed adsorption. Chem. Eng. Technol. 27, 1179–1186. https://doi.org/10.1002/ceat.200407001.

Lu, G., Third, J.R., Müller, C.R., 2015. Discrete element models for non-spherical particle systems: From theoretical developments to applications. Chem. Eng. Sci. 127, 425–465. https://doi.org/10.1016/j.ces.2014.11.050.

Magnico, P., 2003. Hydrodynamic and transport properties of packed beds in small tube-to-sphere diameter ratio: pore scale simulation using an Eulerian and a Lagrangian approach. Chem. Eng. Sci. 58, 5005–5024. https://doi.org/10.1016/S0009-2509(03)00282-3.

Moghaddam, E.M., Foumeny, E.A., Stankiewicz, A.I., Padding, J.T., 2019. Fxed bed reactors of non-spherical pellets : Importance of heterogeneities and inadequacy of azimuthal averaging. Chem. Eng. Sci. X 1,. https://doi.org/10.1016/j.cesx.2019.100006 100006.

Moghaddam, E.M., Foumeny, E.A., Stankiewicz, A.I., Padding, J.T., 2018. Rigid body dynamics algorithm for modeling random packing structures of nonspherical and nonconvex pellets. Ind. Eng. Chem. Res. 57, 14988–15007. https://doi.org/10.1021/acs.iecr.8b03915.

Nemec, D., Levec, J., 2005. Flow through packed bed reactors: 1. Single-phase flow. Chem. Eng. Sci. 60, 6947–6957. https://doi.org/10.1016/j.ces.2005.05.068.

Nijemeisland, M., Dixon, A.G., 2004. CFD Study of fluid flow and wall heat transfer in a fixed bed of spheres. AIChE J. 50, 906–921. https://doi.org/10.1002/aic.10089.

Nijemeisland, M., Dixon, A.G., 2001. Comparison of CFD simulations to experiment for convective heat transfer in a gas-solid fixed bed. Chem. Eng. J. 82, 231–246. https://doi.org/10.1016/S1385-8947(00)00360-0.

Nijemeisland, M., Dixon, A.G., Stitt, E.H., 2004. Catalyst design by CFD for heat transfer and reaction in steam reforming. Chem. Eng. Sci., 5185–5191 https://doi.org/10.1016/j.ces.2004.07.088.

Partopour, B., Dixon, A.G., 2017. An integrated workflow for resolved-particle packed bed models with complex particle shapes. Powder Technol. 322, 258–272. https://doi.org/10.1016/j.powtec.2017.09.009.

Rakotonirina, A.D., Delenne, J.-Y., Radjai, F., Wachs, A., 2018. Grains3D, a flexible DEM approach for particles of arbitrary convex shape—Part III: extension to non-convex particles modelled as glued convex particles. Comput. Part. Mech. 324, 1–30.

Robbins, D.J., El-Bachir, M.S., Gladden, L.F., Cant, R.S., von Harbou, E., 2012. CFD modeling of single-phase flow in a packed bed with MRI validation. AIChE J. 58, 3904–3915.

Seelen, L.J.H., Padding, J.T., Kuipers, J.A.M., 2018. A granular discrete element method for arbitrary convex particle shapes: method and packing generation. Chem. Eng. Sci. 189, 84–101. https://doi.org/10.1016/j.ces.2018.05.034.

Singhal, A., Cloete, S., Radl, S., Quinta-Ferreira, R., Amini, S., 2017a. Heat transfer to a gas from densely packed beds of monodisperse spherical particles. Chem. Eng. J. 314, 27–37. https://doi.org/10.1016/j.cej.2016.12.124.

Singhal, A., Cloete, S., Radl, S., Quinta-Ferreira, R., Amini, S., 2017b. Heat transfer to a gas from densely packed beds of cylindrical particles. Chem. Eng. Sci. 172, 1–12. https://doi.org/10.1016/j.ces.2017.06.003.

Sonntag, G., 1960. Einfluß des Lückenvolumens auf den Druckverlust in gasdurchströmten Füllkörpersäulen. Chemie Ing. Tech. 32, 317–329.

Standish Subagyo, N., Brooks, G.A., 1998. A new model of velocity distribution of a single-phase fluid flowing in packed beds. Chem. Eng. Sci. 53, 1375–1385. https://doi.org/10.1016/S0009-2509(97)00444-2.

Taskin, M.E., Dixon, A.G., Nijemeisland, M., Stitt, E.H., 2008. CFD study of the influence of catalyst particle design on steam reforming reaction heat effects in narrow packed tubes. Ind. Eng. Chem. Res. 47, 5966–5975. 0.1021/ie800315d.

Wehinger, Gregor D., Eppinger, T., Kraume, M., 2015a. Evaluating catalytic fixed-bed reactors for dry reforming of methane with detailed CFD. Chemie-Ingenieur-Technik 87. https://doi.org/10.1002/cite.201400153.

Wehinger, Gregor D, Eppinger, T., Kraume, M., 2015b. Detailed numerical simulations of catalytic fixed-bed reactors: Heterogeneous dry reforming of methane. Chem. Eng. Sci. 122, 197–209. https://doi.org/10.1016/j.ces.2014.09.007.

Wehinger, G.D., Füterer, C., Kraume, M., 2017. Contact modifications for CFD simulations of fixed-bed reactors: Cylindrical particles. Ind. Eng. Chem. Res. 56, 87–99. https://doi.org/10.1021/acs.iecr.6b03596.

Winterberg, Markus, Tsotsas, E., 2000a. Modelling of heat transport in beds packed with spherical particles for various bed geometries and/or thermal boundary conditions. Int. J. Therm. Sci. 39, 556–570. https://doi.org/10.1016/S1290-0729(00)00251-9.

Winterberg, Markus, Tsotsas, E., 2000b. Correlations for effective heat transport coefficients in beds packed with cylindrical particles. Chem. Eng. Sci. 55, 5937–5943. https://doi.org/10.1016/S0009-2509(00)00198-6.

Winterberg, M., Tsotsas, E., 2000c. Impact of tube-to-particle-diameter ratio on pressure drop in packed beds. AIChE J. 46, 1084–1088. https://doi.org/10.1002/aic.690460519.

Winterberg, M., Tsotsas, E., Krischke, A., Vortmeyer, D., 2000. A simple and coherent set of coefficients for modelling of heat and mass transport with and without chemical reaction in tubes filled with spheres. Chem. Eng. Sci. 55, 967–979. https://doi.org/10.1016/S0009-2509(99)00379-6.

Zhong, W., Yu, A., Liu, X., Tong, Z., Zhang, H., 2016. DEM/CFD-DEM Modelling of Non-spherical Particulate Systems: Theoretical Developments and Applications. Powder Technol. 302, 108–152. https://doi.org/10.1016/j.powtec.2016.07.010.

Further reading

Dixon, A.G., Nijemeisland, M., 2001. CFD as a design tool for fixed-bed reactors. Ind. Eng. Chem. Res., 5246–5254 https://doi.org/10.1021/ie001035a.

Mueller, G.E., 1993. Angular void fraction distributions in randomly packed fixed beds of uniformly sized spheres in cylindrical containers. Powder Technol. 77, 313–319. https://doi.org/10.1016/0032-5910(93)85023-3.